CrossMark

# Effects of whispering gallery mode in microsphere super-resolution imaging

Song Zhou[1,2] · Yongbo Deng[1] · Wenchao Zhou[1] · Muxin Yu[1] · H. P. Urbach[3] · Yihui Wu[1]

**Abstract** Whispering Gallery modes have been presented in microscopic glass spheres or toruses with many applications. In this paper, the possible approaches to enhance the imaging resolution by Whispering Gallery modes are discussed, including evanescent waves coupling, transformed and illustration by Whispering Gallery modes. It shows that the high-order scattering modes play the dominant role in the reconstructed virtual image when the Whispering Gallery modes exist. Furthermore, we find that the high image resolution of electric dipoles can be achieved, when the out-of-phase components exist from the illustration of Whispering Gallery modes. Those results of our simulation could contribute to the knowledge of microsphere-assisted super-resolution imaging and its potential applications.

## 1 Introduction

Conventional microscope objective lenses are diffraction limited. Near-field scanning optical microscopy [1] and the super-lens [2–6] based on negative refraction of noble metal-based surface plasmonics can beat the limit; however, they cannot work in far field and are not suitable for wideband spatial spectrum imaging. It has been shown that microsphere lens combined with a conventional microscope can achieve very high resolution for the imaging of non-fluorescent samples or structures [7–21]. Challenges in finding its inherent resolution gain have been done in [22, 23]. The mechanism of this technique is not well known. It is said that the resolution is related to photonic nanojet [7] formed by the microsphere and the transformation of the evanescent waves of the sample into propagating waves [8, 11]. However, it is challenging to resolve two points with the distance less than 100 nm based on vectorial magnetic analysis [24]. Recently, there have been some attentions paid to the effects of Whispering Gallery mode (WGM) for imaging and it stated that WGM is helpful for improving the resolution [25]. In addition, the electromagnetic modes of objects having a crucial role has also been demonstrated in microsphere super-resolution imaging [26, 27].

In this work, two dimensional model is utilized to analytically and numerically investigate the effects of WGM on improving the resolution, with information collected for imaging and special electromagnetic modes of objects caused by illumination. With the solutions of Maxwell's equations and the semi-analytical method with Mie's solution–formulations, the details of high spatial spectrum information being carried into far field and being resolved by the imaging system are described. Furthermore, the situations for higher imaging resolution when the out-of-phase components produced by the illumination are discussed.

## 2 The evanescent waves collected and intensity enhanced transforming by WGMs

The model for calculation is shown in Fig. 1. As the objects to be observed, two incoherent point sources are located below a microcylinder lens whose refractive index is $n_c$ and

✉ Yihui Wu
   yihuiwu@ciomp.ac.cn

1 State Key Laboratory of Applied Optics, Changchun Institute of Optics, Fine Mechanics and Physics, Chinese Academy of Sciences, Changchun 130033, China

2 University of Chinese Academy of Sciences, Beijing 100039, China

3 Optics Research Group, Department of Imaging Physics, Delft University of Technology, Lorentzweg 1, 2628CJ Delft, The Netherlands
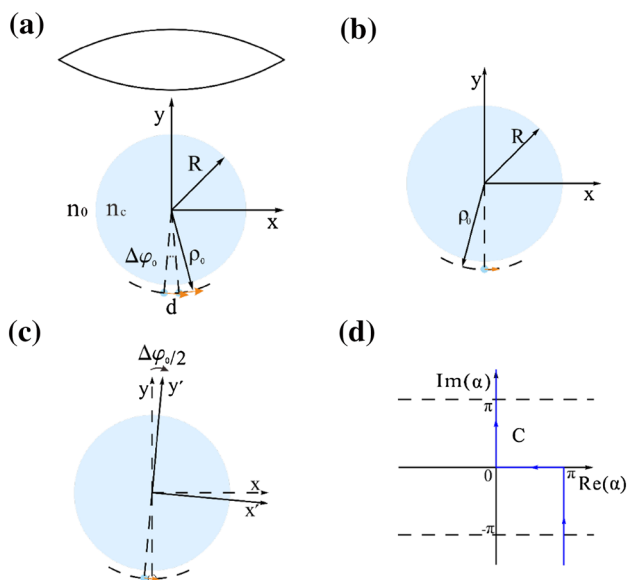
**Fig. 1** **a** 2D model of imaging of two point current sources with arc spacing distance $d = \rho_0 \Delta \varphi_0$. **b** One point current source near a cylinder. **c** Electromagnetic field of the *left* obtained by clockwise rotation of **b**. **d** Integration contour, the region between the *two horizontal dashed lines* is adapted in computational process

radius is $R$ (Fig. 1a). The refractive index of the background is $n_0$. The two point current sources are at position $\left\{ \rho_0, \varphi_0 - \frac{\Delta \varphi_0}{2} \right\}$ and $\left\{ \rho_0, \varphi_0 + \frac{\Delta \varphi_0}{2} \right\}$, which have the same amplitude $j_\varphi = 1$. This model is similar as the model proposed in [19]. The magnetic field in Fig. 1b has only one component $H_z(\rho, \varphi)$ along $z$, and it is expressed as

$$H_z(\rho, \varphi) = \sum_{n=-\infty}^{+\infty} D_n H_n^{(1)}(k_0 \rho) e^{in\varphi} \quad (\rho > \rho_0), \tag{1}$$

where $D_n$ are coefficients. All complex fields and currents have $e^{-i\omega t}$ time dependence.

To make the calculation easier and the results more understandable, the resonances of the cylinder and the virtual images will be obtained by the numerical solutions of Maxwell's equations showed [28], while the quantities of the transformation from the evanescent waves to propagation waves will be obtained by semi-analytical formulations which are presented in the Appendix. The image resolution will be obtained by checking the imaging pattern from rotating one dipole to be close to the other one. The modes distributions, at the exterior of the lens, which could form the image on the far-filed detector are shown in Fig. 2 with a pair of parameters ($n_c = 1.5$, $n_0 = 1.0$, $R = 2.5\ \mu m$, $\rho_0 = 1.002R$). The wavelength will be scanned from 400 to 700 nm and the resonance wavelength here is 425.5 nm, where the WGM presents in the microcylinder. It shows in Fig. 2 that the magnetic intensity of viral imaging of different exterior

modes excited by a single point current source near a cylinder sketched in Fig. 1b. The magnetic intensity along y direction with different exterior modes is shown in Fig. 2e. It shows that the imaging pattern of the exterior higher-order modes appear farther from the center of the lens. The imaging pattern of the exterior modes can be less than half of the wavelength shown in Fig. 2f, and the virtual images of the higher-order modes are more sensitive for intensity distinguishment to the positions of the point source than the lower ones. In Fig. 3, we analyze the model with the high-order mode simulated, shown in Fig. 1a. By comparing the virtual image of WGM resonance with off-resonance showed in Fig. 3, we conclude that the high-order mode plays the dominant role in imaging when WGM excitation occurs. By comparing Fig. 3d, h, the distinguishment of two point becomes well when the high-order mode becomes stronger in the total field.

Using Mie's solution–formulation, we analyze the contribution of near-field evanescent waves by setting the up and low limit of the integration contour, which contains the imaginary part for the source with evanescent wave components; if the near-field evanescent waves are ignored, the imaginary part for the source will not be included in the integration contour (Fig. 1d). In Fig. 4a, b, we give the correlation between the coefficient of one mode and spatial frequency spectrum. We summarize that high spatial frequency has a primary role for high-order modes and an ignored role for low-order modes. We also show the dominant role of the transformation of evanescent waves to propagating waves for WGM excitation, and the scattering mode enhancement of the excited WGM in the remaining figures of Fig. 4.

From these results, we can demonstrate the effects of WGM in the process of collecting information of a point source. Each exterior mode has organized spatial frequency spectrum and can form an imaging pattern with less than half of illumination wavelength. Among these, the exterior mode corresponding to the fundamental WGM could realize higher resolution than the others. And the transformation of evanescent waves to propagating waves can be enhanced when the model meets WGM stimulated, and the corresponding exterior mode can be improved to realize higher resolution.

## 3 Imaging of two nanoparticles under photonic nanojets

The light source is the objects themselves shown in the previous part. However, the illumination can affect the imaging a lot, especially when it may induce the special electromagnetic modes [26]. The two nanoparticles take the place of two point source as the objects and they are illuminated by photonic nonojet (PNJ). For investigating two nanoparticles
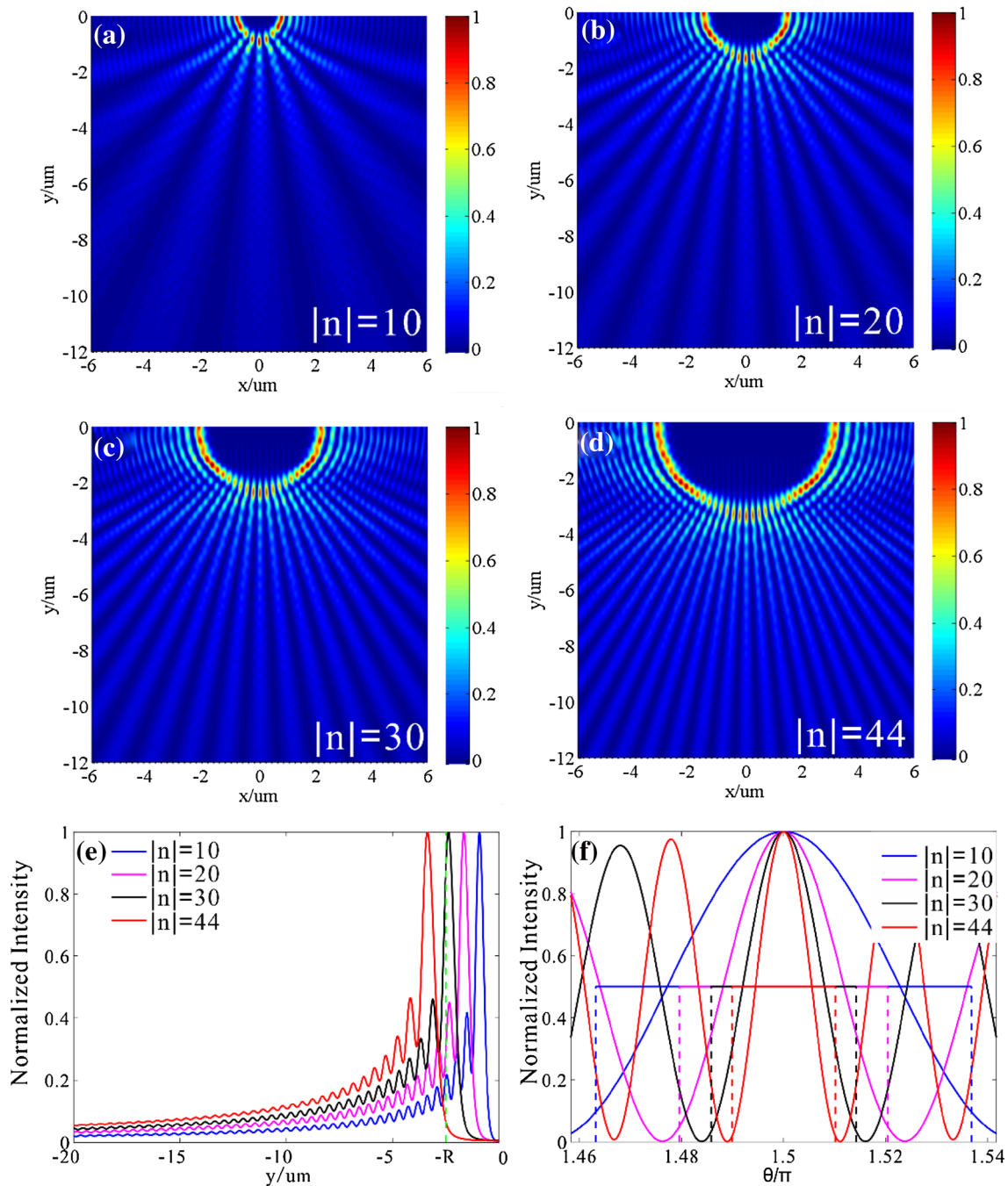
**Fig. 2** The magnetic intensity (squared amplitude of the magnetic field) of viral imaging of different exterior modes excited by a single point current source near a *cylinder* sketched in Fig. 1b, where the mode number corresponding to **a**–**d** are $|n| = 10$, $|n| = 20$, $|n| = 30$ and $|n| = 44$, respectively; **e** normalized magnetic intensity along *y*-axis; **f** normalized magnetic intensity as function of angle $\varphi$ along the *circle* with radius given by the *y* value in Fig. 2e, where the maximum appears (the angular distance between the *dotted lines* of the *same color* corresponds to a distance of $\lambda/2$)

under PNJ, the numerical 2D model is shown in Fig. 5a, a micro-cylinder with a refractive index (RI) of $n_c = 1.5$ is placed in the free space ($n_0 = 1$). The radius $R$ of the micro-cylinder is 1.5 μm, and it is illuminated by a TM-polarized plane wave propagating along the *y*-axis (i.e. its electric field is in the *x*-direction and its magnetic field is parallel to the *z*-direction, which is perpendicular to the plane of drawing). Two nanoparticles are on the shadow side of the micro-cylinder with diameter $d = 80$ nm and a refractive index (RI) of $n_w = 1.6$. The center-to-center distance of the

**Fig. 3** Virtual images of the cases including WGM resonance and off-resonance sketched in Fig. 1a. **a, c, e, g** Normalized modulus coefficients of mode expansion (see Eq. 1) of the magnetic field outside the cylinder; **b, d, f, h** reconstructions of two incoherent point current sources. The *inset figures* in **b, d, f, h** are normalized magnetic intensity along *x*-direction at $y = -7.538$ μm for **b**, $y = -3.739$ μm for **d**, $y = -3.514$ μm for **f** and $y = -2.355$ μm for **h**, and the *two brown arrows* express the imaging of the two incoherent point current sources. Parameters are selected as $\lambda = 420$ nm, $R = 2.5$ μm, $\rho_0 = 1.002R$, $d = \lambda/3$ for **a, b**; $\lambda = 425.5$ nm, $R = 2.5$ μm, $\rho_0 = 1.002R$, $d = \lambda/3$ for **c, d**; $\lambda = 410$ nm, $R = 1.5$ μm, $\rho_0 = 1.002R$, $d = \lambda/3$ for **e, f** and $\lambda = 413.5$ nm, $R = 1.5$ μm, $\rho_0 = 1.002R$, $d = \lambda/3$ for **g, h**
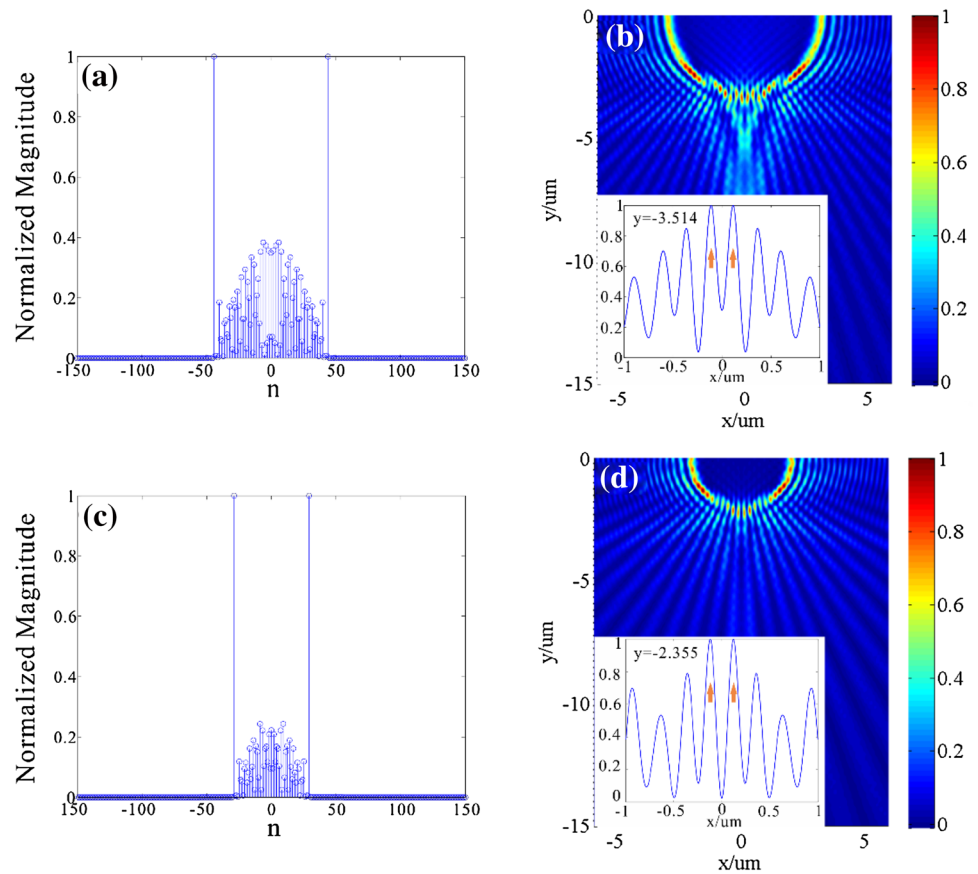


two nanoparticles is $s = 100$ nm. The h shown in Fig. 5a is chosen to be 45 nm. Because the diameter of the nanoparticle is sufficiently small, we may replace the nanoparticle by an electric dipole moment [29], with induced moment given by [30]

$$\mathbf{p} = \varepsilon_0(1 - \varepsilon_r) \int_V \mathbf{E}(\mathbf{r})\mathrm{d}V', \tag{2}$$

where $\varepsilon_0$ is the permittivity of vacuum, $\varepsilon_r$ is relative permittivity of the nanoparticle and $V$ is the volume of the nanoparticle. Let $p_0$ be the normalization factor, defined by

$$p_0 = \left| \varepsilon_0(1 - \varepsilon_r) \int_V E_0 \mathrm{d}V' \right|, \tag{3}$$

where $E_0 = 1$ (V/m).

The finite element software COMSOL Multiphysics [31] is used to compute the illumination of the nanoparticles and the induced re-radiation. The collection of far field is simulated using the open-source code provided in [32]. The virtual image is reconstructed using angular spectrum theory. Figure 5b shows the intensity distribution of PNJ generated by the cylinder at wavelength $\lambda = 550$ nm. Figure 5c shows the intensity distribution of a single nanoparticle under PNJ illumination. Figure 5d shows the equivalent electric dipole moment for a nanoparticle for different positions along *x*-direction. And in Fig. 5e, the intensity distribution of two nanoparticles under PNJ is presented. Because the magnetic field is polarized along the *z*-axis, the equivalent electric dipole moment has components along both *x*- and *y*-directions. For the two nanoparticles with different distances the situations are shown in Fig. 5f. It could be observed that the ratio of the amplitudes of the *y*- and *x*-components of the dipoles' moments vary strongly with the separation distance and the *y*-components of the two equivalent electric dipole moments are found to be out-of-phase while the *x*-components are in-phase. Normally the resolution can be improved effectively, when there is only the out-of-phase component [26]. However, the in-phase component cannot be ignored in practice, and it is usually larger than the out-of-phase component. To make the out-of-phase component dominant, we scan the wavelength in the range from 400 to 500 nm to find the right wavelength. The equivalent electric dipole moment is shown in Fig. 6a. It shows that the *y*-component is larger than *x*-component at suitable wavelength. From Fig. 6a, we select $\lambda = 491$ nm and show
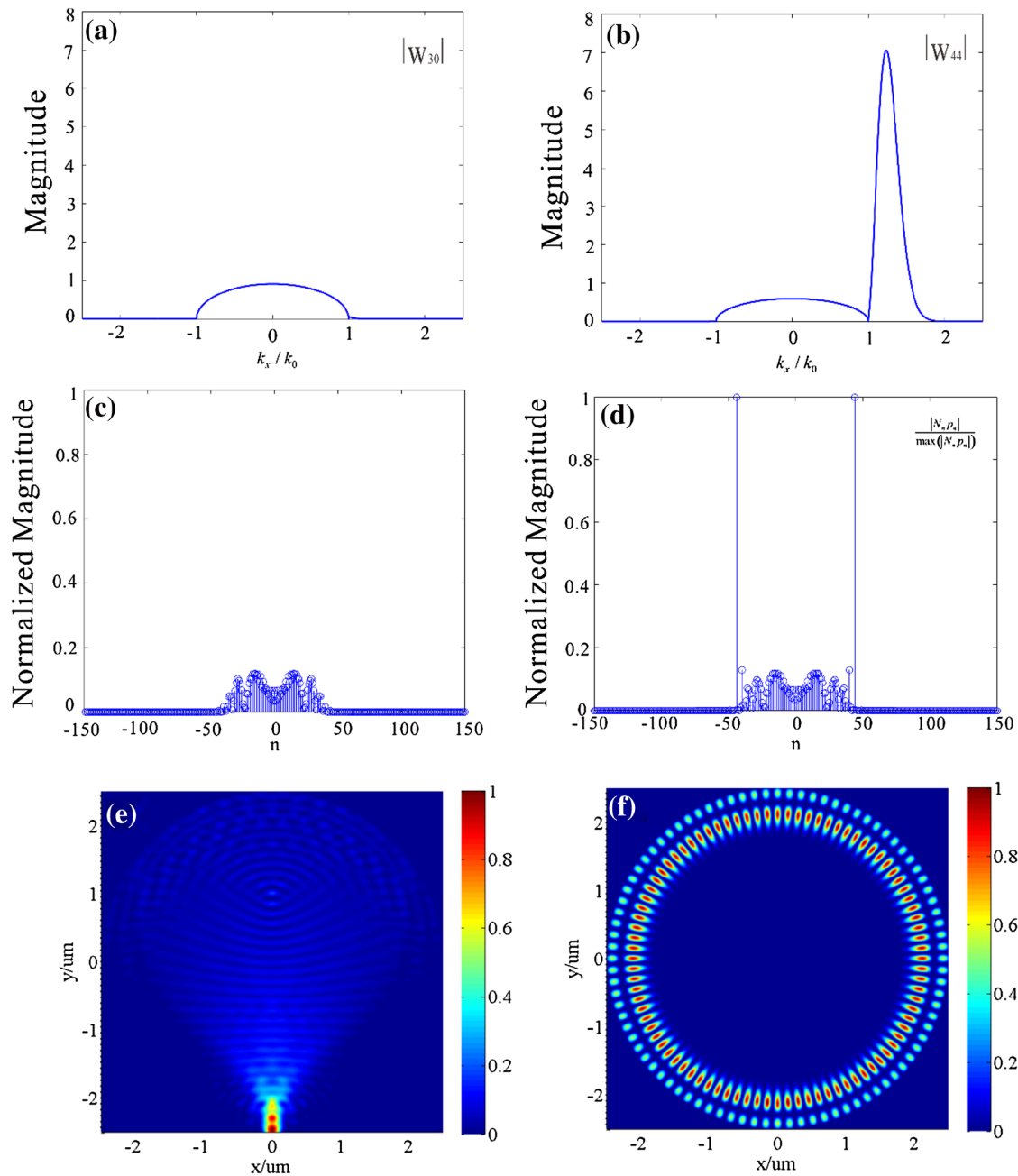
**Fig. 4** The contribution of near-field evanescent waves. **a** $n = 30$, **b** $n = 44$, the resonance mode inside the cylinder. **c** Scattering coefficients considering the point source without near-field evanescent waves (the normalization factor are equal with **d**). **d** Scattering coefficients calculated the point source with near-field evanescent waves. **e** Distribution of normalized magnetic intensity inside the *cylinder* with point source not containing evanescent waves. **f** Distribution of normalized magnetic intensity inside the *cylinder* with point source containing evanescent waves. Where, $W_n = i^n N_n \sin \alpha e^{(-in\alpha - ik_0\rho_0 \sin \alpha)}$, $N_n$ is shown in the Appendix. Parameters are selected as $\lambda = 425.5$ nm, $R = 2.5$ μm, $\rho_0 = 1.002R$

the intensity distribution in Fig. 6b. It could be observed that for this wavelength there is a WGM. This indicates that the WGM can induce that the longitudinal (y-) component of the dipole is dominant. In Fig. 6c, d, we compared the virtual images of the cases with and without WGM. We found an appropriate imaging position to get the two

nanoparticles imaging, as shown by the plotted curve in Fig. 6d. The imaging formed by y-direction point current source under a cylinder is a dark field imaging [33]. We can obtain that the two nanoparticles at $\lambda = 491$ nm with WGM illumination can be distinguished. Due to the fact that the two neighboring standing points have half-wave
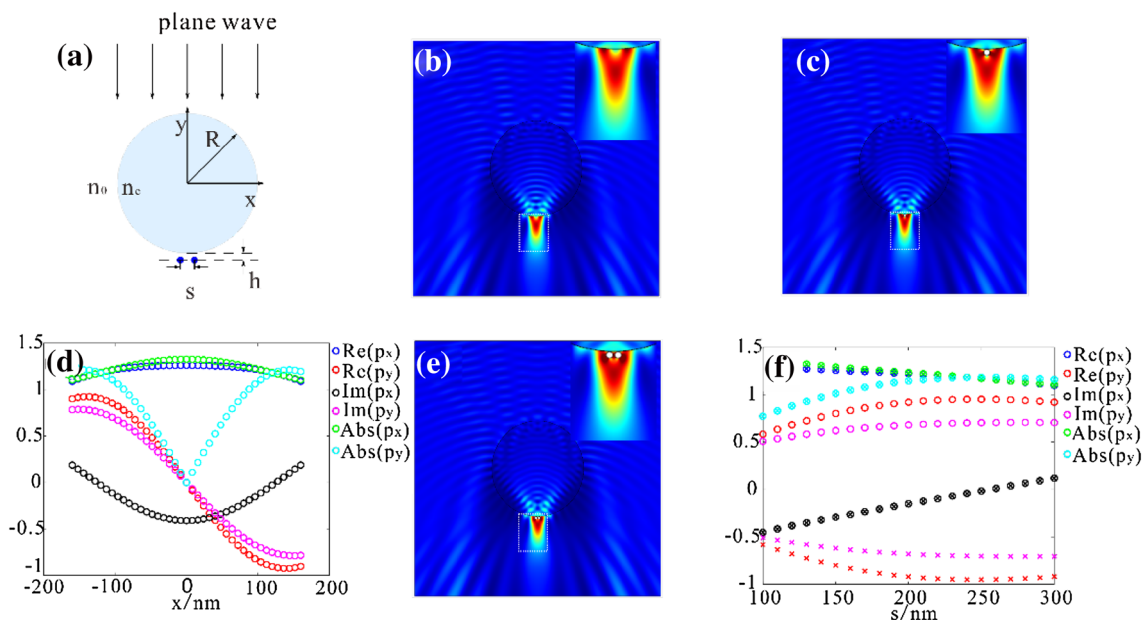
**Fig. 5 a** 2D-configuration with a TM-polarized incident plane wave incident on a *cylinder* and two nanoparticle below the cylinder; **b** optical electric intensity distribution of the PNJ; **c** optical electric intensity distribution of single nanowire under the PNJ; **d** the equivalent electric dipole moment given by **p**/$p_0$ (see Eqs. 2, 3) of a single nanoparticle at different positions; **e** optical intensity distribution of two nanoparticles under the PNJ; **f** the equivalent electric dipole moments of two nanoparticles with different spacing distance ('*o*' left nanowire, '*x*' right one.)

phase difference in the WGM mode, the re-radiation of the observed object can form anti-symmetric mode (out-of-phase component).

## 4 Conclusion

WGM can appear when the white lighting source is used in experiments of microsphere super-resolution imaging. However, the effects of WGM can be "smeared" out by averaging effect the white lighting source [19]. Our results indicate that the increase of high-order scattering mode intensity can improve the resolution of microsphere imaging. And this can be further improved by changing the illuminating method, such as side-illumination or partial inclined illumination in free space [34].

To summaries, we have demonstrated that the high-order scattering mode can form comparatively narrow pattern in the virtual image plane, and the transformation of the evanescent waves to propagating waves can be effectively enhanced by the WGM. Both are crucial effects of the WGM in super-resolution imaging. Furthermore, the out-of-phase components can be achieved in the object due to the focusing performance of the micro-cylinder under a TM-polarized plane wave illumination. And it can be effectively enhanced for the super-resolution less than 100 nm when the WGM is presented.

## Appendix

We start by defining the vector potential $\mathbf{A}(\mathbf{r})$ through [29]

$$\mathbf{H}(\mathbf{r}) = \frac{1}{\mu_r \mu_0} \nabla \times \mathbf{A}(\mathbf{r}), \tag{4}$$

In the Lorenz gauge [35], $\mathbf{A}(\mathbf{r})$ satisfies the wave equation

$$(\nabla^2 + k^2)\mathbf{A}(\mathbf{r}) = -\mu_r \mu_0 \mathbf{J}(\mathbf{r}), \tag{5}$$

In 2D model (shown in Fig. 1b), the wave equation in Cartesian coordinates is

$$\left( \frac{\partial^2}{\partial x^2} + \frac{\partial^2}{\partial y^2} + k^2 \right) A_x(x, y) = -\mu_r \mu_0 j_\varphi \delta(x)\delta(y - \rho_0), \tag{6}$$

Suppose the type of $A_x(x, y)$ is

$$A_x(x, y) = \mu_r \mu_0 j_\varphi \int_{-\infty}^{+\infty} f(k_x) e^{i(k_x x + k_y |y - \rho_0|)} dk_x, \tag{7}$$
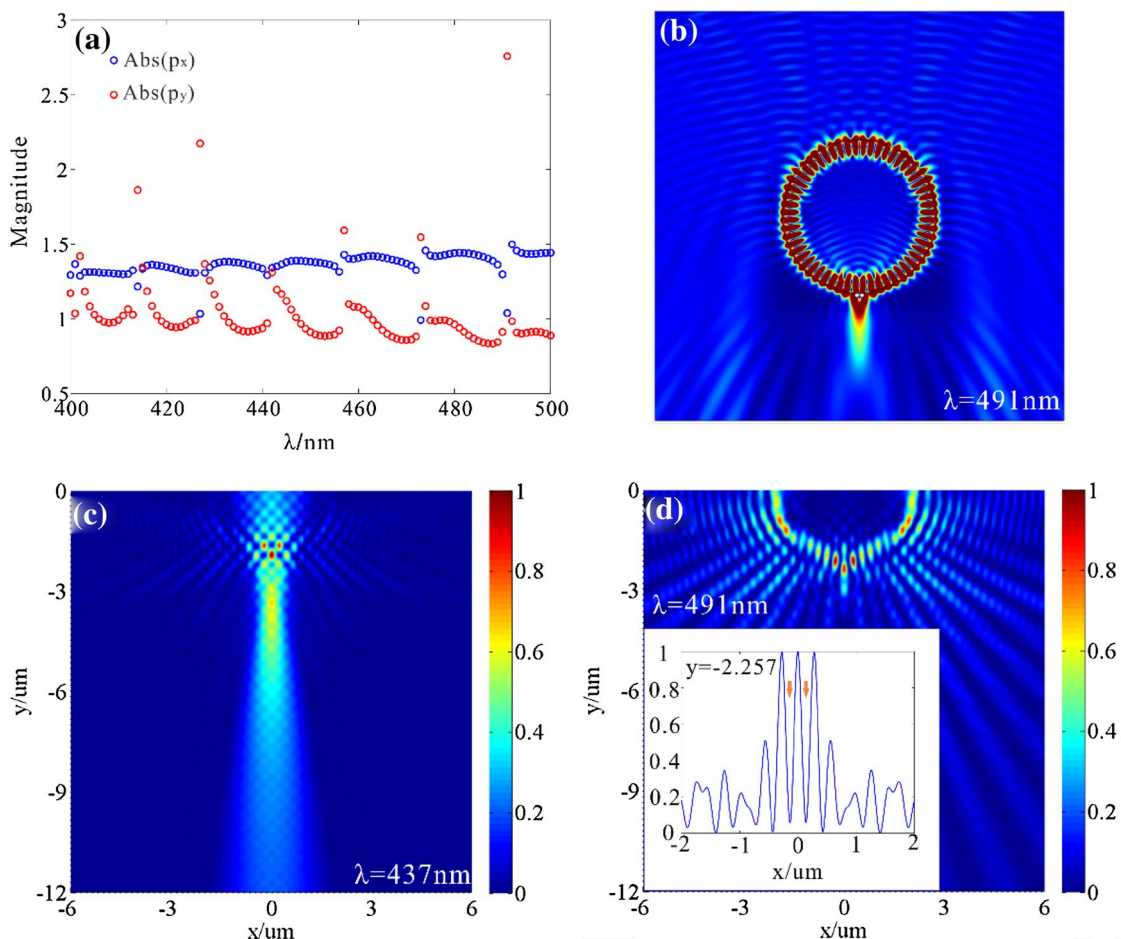
**Fig. 6** **a** The amplitude of the *x*- and *y*-components of the equivalent dipole moment at different wavelength, the separation between the dipoles is 100 nm and the micro-cylinder has radius of 1.5 μm and refractive index 1.6 as before; **b** optical intensity distribution of two nanoparticles under PNJ at optimum wavelength 491 nm; **c**, **d** virtual images of different wavelength of 437 and 491 nm. The *inset figure* in **d** is normalized squared amplitude of the magnetic field along *x*-direction at $y = -2.257$ μm, and the *two brown arrows* express the imaging of the two point current sources

The usual spectral decompositions of the $\delta$ function is

$$\delta(x) = \frac{1}{2\pi} \int\limits_{-\infty}^{+\infty} e^{ik_x x} dk_x. \tag{8}$$

Using these Eqs. (6)–(8), we can get the distribution

$$f(k_x) = \frac{i}{4\pi k_y}, \tag{9}$$

Since the cylinder is above the point current source, the following analysis is under the condition of $y > \rho_0$. Then, we get the magnetic fields and use it as incident field for Mie scattering of the cylinder. From Eq. (4), the incident field is given as

$$H_z(x, y) = -i\frac{j_\varphi}{4\pi} \int\limits_{-\infty}^{+\infty} e^{i(k_x x + k_y(y - \rho_0))} dk_x. \tag{10}$$

To make Mie formulation simplified, we change the representation Eq. (10) into

$$H_z(\rho, \varphi) = ik_0 \frac{j_\varphi}{4\pi} \int\limits_{C} \sin\alpha e^{-ik_0\rho_0 \sin\alpha} e^{ik_0\rho \cos(\varphi - \alpha)} d\alpha, \tag{11}$$

where the integral contour $C$ is shown in Fig. 1d. Using expansion of plane wave in series of cylindrical waves, the incident magnetic field becomes

$$H_z(\rho, \varphi) = ik_0 \frac{j_\varphi}{4\pi} \sum_{n=-\infty}^{+\infty} p_n J_n(k_0\rho) e^{in\varphi}, \tag{12}$$

where

$$p_n = i^n \int\limits_{C} \sin\alpha e^{(-in\alpha - ik_0\rho_0 \sin\alpha)} d\alpha \tag{13}$$

**Fig. 7** Comparison of the numerical and semi-analytical methods. **a**, **c** Normalized absolute values of coefficients of the *cylinder* modes inside the *cylinder* computed by the numerical and semi-analytical method, respectively; in **b**, **d** the *squared* amplitude of the magnetic field is shown inside the *cylinder* as computed by the numerical and semi-analytical method, respectively. The used parameters are $\lambda = 434$ nm, $R = 2.5$ μm, $\rho_0 = 1.002R$, $d = \lambda/2$
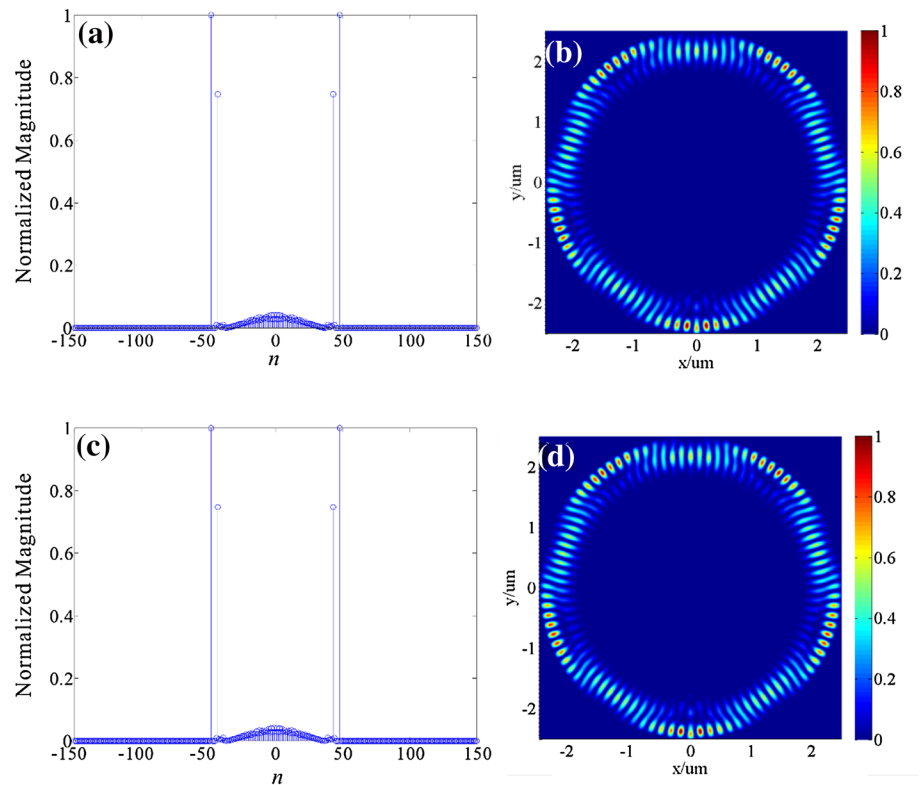
Then, suppose the scattering field and field in cylinder are the following expressions

$$H_z^s(\rho, \varphi) = ik_0 \frac{j_\varphi}{4\pi} \sum_{n=-\infty}^{+\infty} p_n N_n H_n(k_0\rho) e^{in\varphi}, \tag{14}$$

$$H_z^{\text{cyl}}(\rho, \varphi) = ik_0 \frac{j_\varphi}{4\pi} \sum_{n=-\infty}^{+\infty} p_n M_n J_n(k_c\rho) e^{in\varphi}, \tag{15}$$

where the two unknown coefficients $M_n$ and $N_n$ could be solved using the boundary conditions at the interface $\rho = R$, the continuity of $H_z$ and $E_\varphi$. The coefficients are

$$M_n = \frac{H'_n(k_0R)J_n(k_0R) - H_n(k_0R)J'_n(k_0R)}{J_n(k_cR)H'_n(k_0R) - \frac{k_0}{k_c}J'_n(k_cR)H_n(k_0R)}, \tag{16}$$

$$N_n = \frac{\frac{k_0}{k_c}J'_n(k_cR)J_n(k_0R) - J_n(k_cR)J'_n(k_0R)}{J_n(k_cR)H'_n(k_0R) - \frac{k_0}{k_c}J'_n(k_cR)H_n(k_0R)}, \tag{17}$$

Then, we demonstrate that the two analytic simulations have the same results, see Fig. 7.

## References

1. D.W. Pohl, W. Denk, M. Lanz, Optical stethoscopy: image recording with resolution λ/20. Appl. Phys. Lett. **44**(7), 651–653 (1984)
2. J.B. Pendry, Negative refraction makes a perfect lens. Phys. Rev. Lett. **85**(18), 3966 (2000)
3. Z. Jacob, L.V. Alekseyev, E. Narimanov, Optical hyperlens: far-field imaging beyond the diffraction limit. Opt. Express **14**(18), 8247–8256 (2006)
4. Z. Liu, H. Lee, Y. Xiong et al., Far-field optical hyperlens magnifying sub-diffraction-limited objects. Science **315**(5819), 1686 (2007)
5. J. Dong, J. Liu, X. Zhao et al., A super lens system for demagnification imaging beyond the diffraction limit. Plasmonics **8**(4), 1543–1550 (2013)
6. B. Li, B. Hu, Y. Yang, et al., Demagnification imaging improved by mask in a hyperlens photolithography system. Plasmonics **12**(3), 735–741 (2017)
7. Z. Wang, W. Guo, L. Li et al., Optical virtual imaging at 50 nm lateral resolution with a white-light nanoscope. Nat. Commun. **2**, 218 (2011)
8. X. Hao, C. Kuang, X. Liu et al., Microsphere based microscope with optical super-resolution capability. Appl. Phys. Lett. **99**(20), 203102 (2011)
9. L.A. Krivitsky, J.J. Wang, Z. Wang et al., Locomotion of microspheres for super-resolution imaging. Sci. Rep. **3**, 3501 (2012)
10. A. Darafsheh, G.F. Walsh, L. Dal Negro et al., Optical super-resolution by high-index liquid-immersed microspheres. Appl. Phys. Lett. **101**(14), 141128 (2012)

11. L. Li, W. Guo, Y. Yan et al., Label-free super-resolution imaging of adenoviruses by submerged microsphere optical nanoscopy. Light Sci. Appl. **2**(9), 104 (2013)

12. S. Lee, L. Li, Y. Ben-Aryeh et al., Overcoming the diffraction limit induced by microsphere optical nanoscopy. J. Opt. **15**(12), 125710 (2013)

13. A. Darafsheh, Optical super-resolution and periodical focusing effects by dielectric microspheres. The University of North Carolina at Charlotte (2013)

14. Y. Yan, L. Li, C. Feng et al., Microsphere-coupled scanning laser confocal nanoscope for sub-diffraction-limited imaging at 25 nm lateral resolution in the visible spectrum. ACS Nano **8**(2), 1809–1816 (2014)

15. A. Darafsheh, N.I. Limberopoulos, J.S. Derov et al., Advantages of microsphere-assisted super-resolution imaging technique over solid immersion lens and confocal microscopies. Appl. Phys. Lett. **104**(6), 061117 (2014)

16. H. Yang, N. Moullan, J. Auwerx et al., Super-resolution biological microscopy using virtual imaging by a microsphere nanoscope. Small **10**(9), 1712–1718 (2014)

17. A. Darafsheh, C. Guardiola, A. Palovcak et al., Optical super-resolution imaging by high-index microspheres embedded in elastomers. Opt. Lett. **40**(1), 5–8 (2015)

18. F. Wang, L. Liu, P. Yu, et al., Three-Dimensional Super-Resolution Morphology by Near-Field Assisted White-Light Interferometry. Sci. Rep. **6**, 24703 (2016)

19. J.N. Monks, B. Yan, N. Hawkins et al., Spider silk: mother nature's bio-superlens. Nano Lett. **16**(9), 5842–5845 (2016)

20. A. Darafsheh, G. Wu, S. Yang, et al., Super-resolution optical microscopy by using dielectric microwires. SPIE BiOS. International Society for Optics and Photonics, pp. 97130U–97130U-5 (2016)

21. A. Darafsheh, Influence of the background medium on imaging performance of microsphere-assisted super-resolution microscopy. Opt. Lett. **42**(4), 735–738 (2017)

22. A. Darafsheh, C. Guardiola, D. Nihalani, et al., Biological super-resolution imaging by using novel microsphere-embedded coverslips. PIE BiOS. International Society for Optics and Photonics, pp. 933705–933705-7 (2015)

23. A. Darafsheh, Comment on 'Super-resolution microscopy by movable thin-films with embedded microspheres: resolution analysis' [Ann. Phys. (Berlin) 527, 513 (2015)]. Ann. Phys. **528**(11–12), 898–900 (2016)

24. Y. Duan, G. Barbastathis, B. Zhang, Classical imaging theory of a microlens with super-resolution. Opt. Lett. **38**(16), 2988–2990 (2013)

25. T.X. Hoang, Y. Duan, X. Chen et al., Focusing and imaging in microsphere-based microscopy. Opt. Express **23**(9), 12337–12353 (2015)

26. A.V. Maslov, V.N. Astratov, Imaging of sub-wavelength structures radiating coherently near microspheres. Appl. Phys. Lett. **108**(5), 051104 (2016)

27. V.N. Astratov, F. Abolmaali, A. Brettin, et al., Label-free nanoscopy with contact microlenses: super-resolution mechanisms and limitations. Transparent Optical Networks (ICTON), 2016 18th International Conference on. IEEE, pp. 1–4 (2016)

28. A.V. Maslov, M.I. Bakunov, C.Z. Ning, Distribution of optical emission between guided modes and free space in a semiconductor nanowire. J. Appl. Phys. **99**(2), 024314 (2006)

29. L. Novotny, B. Hecht, *Principles of nano-optics* (Cambridge University Press, Cambridge, 2012)

30. D. Sikdar, W. Cheng, M. Premaratne, Optically resonant magneto-electric cubic nanoantennas for ultra-directional light scattering. J. Appl. Phys. **117**(8), 083101 (2015)

31. http://www.comsol.com. Accessed 6 July 2016

32. J. Yang, J.P. Hugonin, P. Lalanne, Near-to-far field transformations for radiative and guided waves. ACS Photon. **3**(3), 395–402 (2016)

33. V.M. Sundaram, S.B. Wen, Analysis of deep sub-micron resolution in microsphere based imaging. Appl. Phys. Lett. **105**(20), 204102 (2014)

34. F. Wang, L. Liu, H. Yu et al., Scanning superlens microscopy for non-invasive large field-of-view visible light nanoscale imaging. Nat. Commun. **7**, 13748 (2016)

35. J.D. Jackson, *Classical Electrodynamics* (Wiley, Oxford, 1999)